Disentangling water, ion and polymer dynamics in an anion exchange membrane

Fabrizia Foglia, Quentin Berrod, Adam J. Clancy, Keenan Smith, Gérard Gebel, Victoria García Sakai, Markus Appel, Jean-Marc Zanotti, Madhusudan Tyagi, Najet Mahmoudi, et al.

Disentangling water, ion and polymer dynamics in an anion exchange membrane

Fabrizia Foglia[1*], Quentin Berrod[2], Adam J. Clancy[1], Keenan Smith[3], Gérard Gebel[2], Victoria García Sakai[4], Markus Appel[5], Jean-Marc Zanotti[6], Madhusudan Tyagi[7,8], Najet Mahmoudi[4], Thomas S. Miller[3], John R. Varcoe[9], Arun Prakash Periasamy[9], Daniel J. L. Brett[3], Paul R. Shearing[3], Sandrine Lyonnard[2*], Paul F. McMillan[1*]

[1] Department of Chemistry, Christopher Ingold Laboratory, University College London, 20 Gordon St., London WC1H 0AJ, UK.
[2] Univ. Grenoble Alpes, CNRS, CEA, IRIG-SyMMES, 38000 Grenoble, France
[3] Electrochemical Innovation Lab, Department of Chemical Engineering, University College London, Torrington Place, London WC1E 7JE, UK.
[4] ISIS Neutron and Muon Source, Rutherford Appleton Laboratory, Harwell Science and Innovation Campus, Chilton OX11 0QX, UK.
[5] Institut Laue Langevin, 71 avenue des Martyrs, CS 20156, 38042 Grenoble CEDEX 9, France.
[6] Laboratoire Léon Brillouin (CEA-CNRS), Université Paris-Saclay, CEA Saclay, 91191 Gif-sur-Yvette Cedex, France.
[7] NIST Center for Neutron Research (NCNR), National Institute of Standards and Technology, Gaithersburg, MD 20899, USA.
[8] Department of Materials Science and Engineering, University of Maryland, College Park, MD 20742, USA.
[9] Department of Chemistry, University of Surrey, Guildford, Surrey, GU2 7XH, UK

Semi-permeable polymeric anion-exchange membranes (AEM) are essential for separation, filtration and energy conversion technologies ranging from reverse electrodialysis (RED) systems that produce energy from salinity gradients [1], fuel cells (FC) to generate electrical power from the electrochemical reaction between hydrogen and oxygen [2-3], and water electrolyzer systems (WE) that provide H_2 fuel [4-5]. Anion exchange AEMFCs and AEMWEs rely on the membrane to transport OH^- ions between the cathode and anode in a process that involves cooperative interactions with H_2O molecules and the polymer dynamics. Understanding and controlling the interactions between the relaxation and diffusional processes pose a main scientific and critical membrane design challenge. Here, quasi-elastic neutron scattering (QENS) is applied over a wide range of timescales (10^0 - 10^3 ps) to disentangle the water, polymer relaxation and OH^- diffusional dynamics in commercially available AEM (Fumatech FAD-55) designed for selective anion transport across different technology platforms, using the concept of serial decoupling of relaxation and diffusional processes to analyse the data. Preliminary data are also reported for a laboratory-prepared AEM especially designed for fuel cell applications.

There is a growing need to develop efficient energy conversion devices using sustainable fuel sources. Polymer electrolyte membrane (PEM) fuel cells that rely on a hydrophobic backbone decorated with ionic side groups to allow selective transport of H^+ or OH^- are one promising technology. The transport mechanisms involve cooperative interactions between the ions, H_2O molecules in the surrounding environment, and relaxation dynamics of the polymer backbone and side groups. Established FCs employ electrocatalytic reduction of H_2 to generate H^+ ions that are transported through the PEM, but they rely on Pt-group-metal-based catalytic nanoparticles to effect the kinetically hindered cathodic oxygen reduction reaction as well as H_2 oxidation. Efforts are under way to develop anion-exchange membrane (AEM) systems that employ more sustainable non-noble metal electrocatalysts [6]. These require efficient OH^- conducting membranes that can withstand highly alkaline

operating environments.

Proton-conducting PEMs derived from Nafion (sulfonated tetrafluoroethylene-based fluoropolymer-copolymers) are widely implemented in present FCs and WEs. Anion-conducting membranes are less well developed but available as specialty products from companies such as FuMA-Tech GmBH [7]. New AEMs incorporating polymer backbones functionalised with quaternary ammonium (QA), imidazolium or guanidinium cations are under development [3,8-11]. The number of water molecules per ionic head group (λ) [12] is critical in determining the anion conduction mechanism. Simulation studies indicate that ionic current flow in AEMs occurs by a combination of vehicular OH^- diffusion and Grotthuss hopping through the H-bonded water network solvated by ionomer side groups (Figs. 1b-d) [13-19]. Changes in water content under operational conditions affect both H_2O and OH^- mobility, and these are both affected by the molecular architecture of membrane ion-conducting channels [16-18,20-22]. The water, ion and polymer dynamics are strongly coupled on picosecond to nanosecond timescales over spatial correlations up to several nm. It is essential to determine the molecular-to-mesoscale transport mechanisms of OH^- in relation to membrane hydration and polymer relaxation dynamics to build the understanding needed for next-generation AEM design.

Quasi-elastic neutron scattering (QENS) provides a powerful technique to study these processes, with its capacity to combine selective chemical and isotopic substitutions using data obtained from instruments with different energy exchange to disentangle various dynamical contributions across ps–ns timescales. Nafion membranes and related model systems have been probed extensively using QENS [23-26]. The Fumasep FA series of membranes is marketed for anion conduction [27-31]. Fumasep FAD-55 studied here is a non-reinforced AEM with high electronic and low ionic resistance stable in alkaline environments up to pH 9 [27]. Previous QENS investigations on related FAA-3 membranes could not establish the OH^- hopping process nor its correlation with water content and polymer dynamics [32-33]. We present a detailed analysis of QENS data for FAD-55 [27-30] in its as-supplied Br- as well as OH/OD- and Cl-substituted forms, over a range of temperatures and hydration levels, using different neutron spectrometers to probe the relaxation and transport dynamics over a wide range of timescales, and disentangle details of the correlated polymer-water interactions and OH^--conductivity mechanism (Figs. 1e-g). The QENS studies are complemented by investigation of polymer degradation occurring when handling OH-forms of the membrane, along with determination of the anionic conductivity correlated with the QENS results. Complementary QENS data were also obtained for a new laboratory-prepared membrane specifically targeted at AEMFC applications (Fig. S8) [34].

Samples and measurement conditions

To evaluate the effects of membrane swelling and water content on the ion mobility, membranes were examined in partially to fully hydrated states expressed in terms of λ to highlight and interpret effects occurring at the molecular to nanoscale, while compensating for ionic exchange capacity (IEC) effects and differences in macroscopic water uptake by different membrane formulations and treatments (Supplementary).

AEMs are susceptible to degradation of the functional groups attached to the polymer backbone in high pH environments especially at low λ values and high temperatures [10,22]. We tested the membrane stability of FAD samples handled under different hydration and thermal conditions in the OH-form by examining the IEC and vibrational (Raman and IR) spectra (Figs. 1h-i). The data were collected on the samples after re-conversion back to the Cl-form after initial handling in the OH-form, and comparing to a Cl-sample that was not

treated with any alkali. We combined our H_2O content determined by thermogravimetric analysis (TGA) constrained by the degradation studies and the IEC results to determine the λ values of different hydrated membranes, showing no significant degradation (<20%; Fig. S2) when FAD was handled in its OH-form at λ>3 at room temperature, as indicated by the relative intensities of the Raman peaks at 1018 and 1412 cm^{-1} due to *N*-methylimidazolium side-groups [35]. These λ values correspond to operational hydration levels achieved within AEMFCs that are not operating at high current densities (Figs. 1h-l; Supplementary text 1) [36]. We did not observe any significant carbonation occurring during sample preparation for QENS studies (Fig. S4), nor any modification of QENS profiles before T-scans in the range 2-325 K (Figs. S16a-e).

Significant degradation (>70%; Supplementary text 1) only occurs after prolonged (≥10 hrs) treatment under harsh alkaline conditions for dehydrated membranes at ≥40°C. After treatment under these condititions (λ=2) TGA results for the degraded membrane indicated a ~2 wt% weight loss below 400 K corresponding to two water molecules that remained strongly H-bonded to the OH^- group in the nominally dried sample, providing insight into understanding the OH^- transport mechanism in intact OH-membranes at higher λ values, discussed below (Fig. S1). Weight losses observed at higher T are associated with thermal degradation of the QA groups and polymer backbone [37].

Chemically and isotopically substituted versions of FAD-55 and its hydrating medium were examined: i) the sample in its as-supplied Br-form hydrated in either D_2O or H_2O; ii) the membrane in OH-form hydrated in H_2O; iii) the AEM sample in OD-form hydrated in D_2O (Figs. 1j-m). The fully deuterated contrast (OD/D_2O) was designed to focus on polymer backbone relaxation, including QA methyl side group rotation (Fig. 1c). The fully hydrogenated (OH/H_2O) sample targeted water (at λ=13) and OH^- facilitated hopping dynamics that were revealed at high-energy resolution. Comparisons with the Br/D_2O and Br/H_2O data allowed us to evaluate potential effects of OH^- nucleophilic attack on the QA side groups, that are considered to be a primary cause of degradation in AEM performance especially at low hydration [3,10,21,38]. A newly-prepared membrane (HDPE-VBC-TMA) [34] was also examined at λ=4 in $OH\text{-}H_2O$ (Fig. S8), focusing on high-resolution experiments (IN16B) to directly show the facilitated OH^- hopping mechanism observed for FAD. Samples had been previously tested for water uptake as well as for alkaline resistance, with IEC decreases <10% when the membrane is dehydrated to λ=4 in OH-form [34][1]. Neutron scattering experiments were performed at different instruments with complementary resolution to disentangle the interacting contributions to the polymer, H_2O and OH^- dynamics[2].

Different dynamic regimes and relaxation processes revealed by EFWS/IFWS

Elastic and Inelastic scattering intensities were analysed using Fixed Window Scans (EFWS/IFWS) by increasing (IN16B, HFBS, IN6-Sharp) or lowering (IRIS) temperature (*T*) between 2-325 K. EFWS data and mean square atomic displacements (*msd*) extracted by

[1] Preliminary results are presented here for comparison with the FAD-55 data: a detailed analysis of the dynamical properties of this new membrane will be reported elsewhere (F. Foglia, A. P. Periasamy et al., in prep.).

[2] Instruments and facilities: the ISIS Neutron and Muon Spallation Source (Harwell, UK), the Institut Laue Langevin (ILL, Grenoble, France), and the NIST Center for Neutron Research (Gaithersburg, USA) using i) high-resolution backscattering (BS) spectrometers IN16B (ILL) and HFBS (NIST) (E_{res}=0.75, 1 μeV: ~0.07-3 ns); ii) the time-of-flight (TOF) near-BS spectrometer IRIS (ISIS) (E_{res}=17.5 μeV: ~5-100 ps); iii) the IN6-Sharp (operated by the Laboratoire Léon Brillouin at ILL) TOF spectrometer (E_{res}=70 μeV ~0.5-20 ps) (Figs. 1e-g).

Debye-Waller analysis are shown in Figure 2, with complementary IFWS data provided in Supplementary Information, giving insight into the sequential activation of different dynamical processes as a function of *T*. As each process (*i*) becomes activated at T_i, the elastic intensity drops accompanied by a corresponding increase in inelastic intensity so that the onset of different dynamic processes is revealed by slope changes in the EFWS and IFWS intensity profiles. These EFWS/IFWS variations are modulated by the finite energy or timescale resolution available to each spectrometer, with the dynamics becoming either too fast or too slow compared with the observational window. Analysis of the datasets obtained across the different instruments thus permits recognition of different dynamic regimes and relaxation behaviours as a function of temperature across all AEM samples and hydration states (Fig. 2).

Region 1 (<200 K) is characterized by a regular loss in EFWS intensity accompanied by an msd increase up to ~200 K, with average slope $d\langle u^2\rangle/dT$~7.4±0.8 10^{-4} Å^2 K^{-1} for λ=4 (IN16B, HFBS, IRIS), increasing to 13.4±0.2 10^{-4} Å^2 K^{-1} when examined within the fast (0.5-20 ps) timescale window of IN6-Sharp. We assign these effects excited at low temperature to fast rotations of -CH_3 groups attached to the polymer [39]. The larger msd change recorded at IN6-Sharp occurs as additional large-amplitude and acoustic-type motions of the polymer backbone contribute to the excitation profile.

In region 2 (>200 K) we observe a rapid EFWS decrease accompanied by a sharp msd rise for H_2O-hydrated samples (λ=4; Fig. 2a), along with an IFWS intensity maximum recorded at IN16B (Fig. S5). This apparent maximum arises as the probed dynamics enter the backscattering window at ~200 K, to reach an energy-dependent maximum at ~260 K, and then vanish at higher *T* as the motional timescales became faster than the observational window. The relaxation time (τ) for this feature is independent of the scattering correlation length (*Q*) indicating a spatially localized process, as is found for the -CH_3 rotational excitations discussed above, but on a slower timescale. Because analogous behaviour is observed for different AEM hydration levels as well as for OH/H_2O and Br/D_2O samples, we can assign these additional features to activation of fast polymer side-chain dynamics occurring on a few ps timescale.

Region 3 is recognised by a sudden drop in EFWS intensity beginning at 250 K, clearly visible across the entire range of slower (IN16B/HFBS, Figs. 2a,c), intermediate (IRIS, Fig. 2b) to fast (IN6-Sharp, Fig. 2d) timescale measurements. The activated process shows a *Q*-dependency at low-*Q* indicating a contribution from centre-of-mass (*c-o-m*) mobility of the species involved. The EFWS changes are more pronounced for H_2O- than D_2O-hydrated samples (Fig. 2b), with the number of mobile species proportional to the hydration state. An accompanying increase in IFWS intensity above 250 K is likewise dependent on the hydration state and isotopic composition (Supplementary Information). We assign this additional *Q*-dependent process to rotational-translational water dynamics activated within hydrated AEM samples.

Region 4 is first observed as a moderate but regular decrease in EFWS intensity for the λ=4 sample measured on IN16B above *T*~270 K, accompanied by a continued msd increase with reduced slope (Fig. 2a). Similar changes are observed for λ=13 at HFBS (Fig. 2c). These observations indicate activation of a further dynamic process occurring on a much slower timescale than those described above. The IFWS signal is *Q*-invariant (Fig. S5) indicating localized dynamics. We assign this additional process to ion hopping facilitated by the remaining H_2O molecule bridging two OH^- groups revealed by TGA. It is only clearly detectable on high-resolution spectrometers, where although both polymer motions and

roto-translational water dynamics remain active, these have become too fast to be observed as discrete contributions to the EFWS and IFWS within the resolution window available to lower-resolution instruments.

Relaxation processes revealed by QENS analysis in the energy exchange domain

We analyzed QENS contributions to datasets plotted in the energy domain between 230-325 K and 4≤λ≤13 by fitting Lorentzian functions guided by the EFWS, msd and IFWS results described above (Fig. 3; analysis details in Supplementary Information). We first describe the fast (1-4 ps) *Q*-independent polymer backbone and side-chain dynamics for samples containing no mobile protons in the ionic phase (D_2O-hydrated samples on IRIS and IN6-Sharp) [40] (Figs. 3a-d). These localised dynamics present above 230 K with an activation energy $E_{A,polymer}$~6.3 kJ mol^{-1} display a decrease in $\tau_{polymer}$ with increasing temperature with enhanced slope for higher hydration levels (Fig. 3c,d). Because these dynamics are present for all samples this contribution was constrained to be a common component for all the analyses.

In high-resolution (e.g. IN16B: E_{res}=0.75 μeV) datasets this contributes to a broad underlying QENS background (i.e. polymer dynamics as detected at IRIS and IN6-Sharp and present at all λ and T values ; Supplementary text 2.2). Water relaxations also contribute to this broad signal. However, the most important feature is the presence of a *Q*-independent Lorentzian signal of much smaller width (a few μeV, equivalent to ~270 ps). The origin of this component was identified by comparing OH- and Br- datasets (Supplementary text 2.2) and assigned to slow OH^- hopping dynamics assisted by H_2O molecules bridging two OH^- (Figs. 3e-i) [17]. This latter contribution was first detected for λ=4 samples at lower temperature (230 K; Fig. 3f), and was maintained at higher hydration levels where the broad background contained contributions from both polymer and H_2O relaxations (Figs. 3f,g). The OH^- residence time ($\tau_{hopping}$) and mean hopping distance (2σ) were determined from the *Q*-independent QENS half-width at half-maximum ($\tau_{hopping}=\hbar/\Gamma$) and intensity ($I$=(1-exp(-$Q^2\sigma^2$)) (Figs. 3h,i) [24]).

Analysis of the data indicated a pronounced *T*-dependency between 230-325 K with an average activation energy E_A=4.0±0.2 kJ mol^{-1} (depending on the hydration state) accompanied by an increase of the hopping distance 2σ between 1.8-2.8 Å (Figs. 3h,i). Increasing hydration from λ=4-13 led to a reduction in $\tau_{hopping}$ between 270-200 ps associated with longer (2.6 *vs* 3 Å) jump distances (Figs. 3h,i). These results agree with simulations indicating a combination of ballistic, sub-diffusive/rattling and diffusive components of OH^- transport dynamics operating in different but overlapping time regimes [15,19]. The determined values of $\tau_{hopping}$ and 2σ, especially at λ=4. They indicate that on the IN16B timescale mainly OH^- 'rattle and hop' events are being probed, with minimal coupling to longer-range molecular/anionic mobility mechanisms [41]. When probed with a faster time window (e.g. IRIS/IN6-Sharp) the facilitated OH^- hopping becomes undetectable, as this component becomes incorporated into the elastic line, while the polymer fast-relaxation component is complemented by a further Lorentzian signal. This new feature is associated with dynamics of included water molecules (Fig. 3j), and its behaviour evolves as a function of hydration levels. At λ=4 (Fig. 3k) it shows *Q*-independent behaviour, compatible with localized (i.e. confined) dynamics (τ~10 ps and E_A~8.4 kJ mol^{-1}; Fig. 3m). By λ=13 (Fig. 3j) the water dynamics have become *Q*-dependent, indicating translationally mobile H_2O (Fig. 3n). We note that in all these cases an additional approximately linear or extremely broad Lorentzian background was needed to account for very fast (sub-ps) relaxations extending from the vibrational regime.

Our QENS analyses correspond to the interpretation of the EFWS/msd/IFWS datasets above

by describing separate but coupled dynamical regimes and relaxation phenomena, that enter the relaxation profile probed by QENS for isotopically- and chemically-substituted AEM samples, exposed to H_2O/D_2O solvents, as a function of hydration levels and temperature. These include i) polymer side-chain and backbone dynamics that operate for all samples throughout the temperature range; ii) localized water motions associated with hydrating H_2O molecules facilitating release of OH^- ions from active polymer sites [15] combined with iii) bulk-like diffusion and rotovibrational dynamics of H_2O molecules with a threshold around λ~8. This progression of water dynamics is rationalized in terms of activation of diffusive motions as mobility channels increase in size and connectivity. Our data agree with simulations predicting large water clusters that could support confined molecular diffusion above λ=8 [10]. Calculated changes in OH^- diffusivity between λ=2.5-4 reflect a transition between aqueous clusters where lack of network connectivity limits long-range diffusion to an enhanced diffusivity regime following formation of an extended H-bonded network [42]. Previous QENS analyses of Fumasep FAA showed bulk H_2O diffusion occurring above λ~5 [32-33].

Analyzing the intermediate scattering function to disentangle different relaxation timescales

The measured scattering datasets *S(Q,ω)* were Fourier-transformed to obtain the full intermediate scattering function *I(Q,t)* extending between ~0.5-3000 ps (Fig. 4; Supplementary text 2.5). This allows an overall view of the sequential processes occurring with different onset temperatures and relaxation dynamics and reveals the coupling between them. This analysis parallels that applied to "serial decoupling" of relaxational and diffusive modes for glass-forming liquids and ion-conducting polymers [43-44]. The combined *I(Q,t)* profiles from different instruments reveal clear changes in slope at ~20 and 100 ps, as the dynamic signatures from fast-relaxing polymer motions are followed by H_2O translational and then slower facilitated OH^- hopping processes enter the relaxation profile (Fig. 4a; Fig. S20). The data for different *Q* values are shown for the instruments probing different timescale ranges in Figs. 4b-d.

Focusing on the λ=4 sample studied at 230 K, it first develops a plateau at ~100 ps followed by a shallower *I(Q,t)* reduction to longer timescales (Figs. 4e,f). This sample exhibits a change in *Q*-dependency at slow timescales with an inflection at ~2000 ps (0.6-1.3 $Å^{-1}$; Fig. 4g), revealing 'rattling' motions over nearest neighbour (~3 Å) distances. The results indicate species localized within cage sites, that could have the ability to diffuse over longer (i.e., exceeding the probed window) timescales [45]. Above 280 K, the plateau almost disappears (Fig. 4f) and the entire curve shifts towards shorter timescales (Fig. 4e). The transition between the two behaviours (278 K) sets a limit between facilitated hopping *vs* diffusion processes controlling the transport and thus dominating the scattering profile, as found for supercooled liquids [46].

The data also highlight an additional underlying component that enhances the facilitated hopping mechanism and eventually dominates the scattering profile above 280 K. This component, visible on the IRIS timescale (Fig. S12), could be responsible for the IFWS *Q*-dependence at very low-*Q* (Figs. S5-6). It might well result from interconnectivity developed between water domains [47] and formation of a hydrogen-bonded network, that are both essential for efficient FC operation [42]. Under fully hydrated conditions, diffusive transport begins to dominate the coupled process, as evidenced by the *Q*-dependence of *I(Q,t)* at faster timescales (Fig. S20). The implementation of the timescale decoupling approach further permits the identification of a long-range component around one order of

magnitude slower that leads to the *I(Q,t)* decay observed into the ns regime, as well as to the quantification of fast *vs* slow mobile fractions. The "slow" population includes counting two protons per dynamic event, due to one water molecule bridging between QA polymer side-groups and facilitating the OH^- hopping mechanism (Fig. 5a).

Relationships of nanoscale dynamics to OH^- conductivity

We measured ionic conductance for FAD in different ionic forms to compare with our QENS analysis (Fig. 5; Fig. S3). A main factor determining anionic mobility concerns the structural integrity of the polymer backbone and ionomeric side groups under the highly alkaline conditions and elevated temperatures during operation. Our degradation studies indicate that FAD-55 maintains its polymeric and side-chain structure at T<40°C under alkaline conditions for λ=4 and above. AEMFCs are expected to function at higher temperature (>60°C and up to 80-95°C), for which more pH- and T-resistant membranes are now being designed and tested [48]. FAD-55 exhibited a noticeable loss in conductivity when operated under low-hydration (λ=4) and high-T (>40°C) conditions as expected from the degradation results.

The anionic conductivity is also known to be affected by potential reaction of the OH^- groups with atmospheric or dissolved CO_2 causing the formation of (bi)carbonate species especially under low-hydration conditions [49-50]. We carefully excluded CO_2 from the sample chambers for our QENS experiments, and FTIR data taken for samples following similar preparation and analysis protocols showed no evidence for these species (Fig. S4). Our conductivity results found the OH^- mobility to be approximately twice that of Cl^- Fig. S3).

The degree of water uptake controls the delicate balance between vehicular *vs* hopping transport mechanisms as discussed above [17,47]. Computational studies show that as a consequence of electro-osmotic drag, water is partitioned unevenly within the cell along the trajectory between cathode and anode (Fig. 5a) [51]. Under fully hydrated conditions, the coupled process is dominated by vehicular transport with D_{tr} comparable to the total diffusion coefficient for membranes similar to FAD [15-18]. The simulations further indicate a long-range component comparable to the value computed for OH^- diffusion [15-16], suggesting that the Grotthuss mechanism contributes ~15% to the total process.

The activation energy E_A=24.5±4.5 kJ mol^{-1} for coupled OH^-/H_2O diffusion determined by QENS is comparable with that from conductance (17.3±0.1 kJ mol^{-1}; Fig. 5b). The higher conductivity is related to the different effect of the hydration shell around the anions, with H-bonding between OH^- and H_2O facilitating diffusion and proton hopping. As the hydration level is lowered to λ=8, representing a typical overall water content within an AEM polymer matrix under normal operating conditions [51], the self-diffusion coefficient becomes ~50% slower than at λ=13 (Fig. 5c). A smaller (~10%) conductivity variation is found when comparing with operation at similar temperatures (Fig. 5c). This result suggests that vehicular transport provides the main contribution to the anion conductivity at high hydration levels. Above λ=8 we expect that channels with bulk water facilitate vehicular diffusion of the anions. At λ=4 and below, water mediated OH^- hopping becomes the primary component of the coupled transport mechanism, with a limited contribution from vehicular transport activated above 280 K, as demonstrated by the IRIS QENS datasets and *I(Q,t)* observed at fast timescales (Figs. 4e-f), as well as by the remarkable reduction in conductivity by around one order of magnitude (Fig. 5c). This reduction cannot be ascribed to membrane degradation as complete recovery of the conductivity is observed at 303 K (Fig. S3b); it is, therefore, due to suppression of ion structural diffusion as well as a lower degree of dissociation (as observed in proton conducting materials).

Our results indicate that OH^- transport *via* Grotthuss H^+ hopping is enabled within a dynamic complex with three “fast” and one “slow” H_2O molecules bridging two OH^- groups, corresponding to the structural configuration suggested for the strongly bound remnant water found by TGA for our fully dried "reference" sample. These three H-containing species must be doubled in number to activate the complementary mass transport process. Our diffusion results at low hydration, where OH^- has only its first hydration shell completed, are consistent with the model proposed by Zelovich et al. [19].

Conclusions

Our results provide new insights into OH^- transport dynamics relevant to the operation of AEMFCs and other devices. They support previous simulations indicating that charge transport occurs by a combination of vehicular OH^- diffusion and Grotthuss H^+-exchange with the two mechanisms balanced according to the hydration level [13-18,52]. The reduced efficiency of anion transport at low-hydration is due to the absence of coupling with H_2O diffusional dynamics enabled at higher hydration, rather than degradation of ionomer functionality. The fact that the dynamics are associated with two slow protons indicating the need for one H_2O molecule to mediate the OH^- transport explains why the slower vehicular mechanism dominates at low-hydration. At medium-hydration the conductivity is determined by water mobility slowdown through interactions with the polymer matrix, whereas at high-hydration the diffusivity is dominated by bulk water dynamics. The insights provided by these data provide a guide for the design of new devices, where tuning the membrane nanostructure would result in activation of the anionic hopping mechanism, providing improved performance over a wide range of operational conditions.

Acknowledgments: We thank the neutron scattering facilities at ILL (Grenoble, France), ISIS (UK), and NIST (USA) for the award of beamtime necessary to carry out these experiments. We are grateful to ISIS (Didcot, UK) and ILL (Grenoble, France) for neutron beamtime (DOI: 10.5286/ISIS.E.RB1920608, 10.5286/ISIS.E.RB2090038-1 and 10.5291/ILL-DATA.9-11-1916). We also thank Science and Technology Facilities Council (STFC) for the use of Nano-inXider instrument in the Materials Characterisation Laboratory. Access to the HFBS was provided by the Center for High-Resolution Neutron Scattering, a partnership between the NIST and the NSF under agreement no. DMR-1508249. Certain commercial equipment, instruments, or materials are identified in this paper in order to specify the experimental procedure adequately. Such identification is not intended to imply recommendation or endorsement by the NIST.

Funding: This project has received funding from the EU Graphene Flagship under Horizon 2020 Research and Innovation program grant agreement no. 881603-GrapheneCore3 and from the EPSRC Materials Research Hub for Energy Conversion, Capture, and Storage (M-RHEX) EP/R023581/1. AJC thanks SCI and the Ramsay Memorial Trust for support. Degradation studies performed at Surrey University were funded by EPSRC grants EP/M022749/1 and EP/T009233/1.

Author contributions: The study was initiated as a collaboration between CEA and UCL at a meeting between PRS, FF, PFM, SL, GG, QB and JMZ, following discussions with DJLB and TSM. Neutron scattering experiments were initiated and directed by FF and SL in collaborations with VGS, QB, JMZ, MA and MT at neutron beamline facilities. AJC and KS also participated in neutron scattering experiments, KS carried out ionic conductivity

experiments under supervision from TSM, DJLB and PRS, AJC provided FTIR and TGA data and NM obtained essential SAXS/WAXS and SANS data. FF and PFM worked closely with SL and QB to interpret the neutron scattering results. Sample degradation, IEC determinations and Raman spectroscopy experiments were initiated and carried out by JRV and AP. All authors read, edited, commented on, and fully contributed to developing the study and this manuscript.

Competing interests: The authors declare that they have no competing interests.

Figure legends/captions

Fig. 1 | Schematic illustration of AEMFC and the FAD-55 AEM in relation to measurement protocol. a, Schematic illustration of an AEMFC and its mode of operation. **b-d**, Sketches illustrating the polymeric membrane, the facilitated OH^- hopping mechanism, and water translational dynamics and interactions between these dynamic processes. The cartoon at right shows rapidly relaxing -CH_3 species attached to the polymer backbone [9] and functional groups [8-10,35]. Note that here we have presumed a structural model for the side group functional groups based on our Raman spectroscopic analyses [35]. **e-g**, Timescales probed in neutron scattering experiments at instruments with different energy resolution characteristics. **h**, Raman spectra recorded on a sample of FAD in its Cl-form (red spectrum, where the FAD sample had not been exposed to any high pH or low hydration conditions) and a sample in the Cl-form after it had been dehydrated at λ=4 in the OH-form (green spectrum); spectral intensities normalized to the * peak to aid visual comparison. **i**, Ion-Exchange Capacities (IEC) for Cl-form FAD samples after they had been treated to different hydration states in the OH-form (green and grey bars; dehydrated at room temperature and 40°C, respectively) compared to its Cl-form (brown dotted range). **j-m**, chemically/isotopically substituted AEM/hydration medium combinations used to investigate different aspects of the dynamics.

Fig. 2 | EFWS Intensity and Mean Squared Displacement (msd) data for FAD-55 Membrane. Profiles were been recorded for FAD-55 at different hydration levels (λ=4,13) and isotopic compositions (OH/H_2O and Br/D_2O) at instruments with different E_{res}. The datasets are separated according to hydration level. **a-b**, low-hydrated samples (λ=4). **c-d**, fully-hydrated samples (λ=13). Data obtained at each instrument are designated by different panel outlines: i) 0.75 μeV (high resolution - IN16B; solid light blue); ii) 1.0 μeV (high resolution - HFBS; dashed light blue); iii) 17.5 μeV (intermediate resolution - IRIS; solid blue) and iv) 70 μeV (broad resolution - IN6-Sharp; dark blue). OH/H_2O-hydrated samples (e.g. OH-form) are reported as blue (λ=13) and green (λ=4) symbols; Br/D_2O-hydrated samples (e.g. Br-form) are designated by red (λ=13) and orange (λ=4) symbols. Information extracted on mean square displacements (*msd*) are provided at right in each panel. The msd slope extrapolated from data at low-*T* is shown as a black line. The plots are used to highlight four dynamic ranges of interest: 1) -CH_3 polymer dynamics; 2) side-chain polymer dynamics; 3) water dynamics and 4) facilitated ion hopping. Corresponding IFWS data and analysis details are provided in Supplementary Information.

Fig. 3 | Analysis of QENS associated with different dynamical processes; data for FAD-55 Membrane. a, 424 Schematic illustration of polymer dynamics incorporating methyl group pseudorotation and other fast (1-4 ps depending on hydration state) side chain and backbone dynamics activated above T~230 K. **b**, Analysis of the signal obtained at T=300 K for a λ=4 OD/D_2O sample using Eres=17.5 μeV (intermediate resolution - IRIS). The instrument resolution function is shown as a solid blue line underneath the data points (open squares). The fast polymer relaxation gives rise to an extremely broad Lorentzian contribution (grey shaded area) underlying the data. The convolution of the two is shown as the red line fitting through the data points. **c**, relaxation times ($\tau_{polymer}$) for the polymer dynamics extracted from the QENS linewidths for OD/D_2O samples with different hydration levels (λ=4-13) between T=230≤T≤335 K. **d**, $\tau_{polymer}$ values determined for Br/D_2O samples at 300 K as a function of hydration level (λ=0-13). **e**, Schematic illustration of slow (200-500 ps) facilitated OH^- ion hopping dynamics that can either be mediated by vehicular transport of OH^- ions or Grotthuss H^+ transport involving depending on the hydration level of the AEM. **f,g**, Scattering profiles at λ=4 for OH/H_2O samples at 230 and 300 K, respectively, measured at IN16B (high resolution). The narrow Lorentzian signal (mauve shaded area) represents the facilitated OH^- hopping dynamics superimposed on a very broad background (light blue)

corresponding to underlying polymer + H_2O dynamics, that occurs on too rapid timescales to contribute to the narrower Lorentzian function within the instrumental E_{res} (0.75 μeV). Symbols and lines for the experimental data (squares), instrumental resolution function (blue) and global fit (red) are as before. **h**, Facilitated hopping dynamics timescale (τhopping) extracted from QENS linewidths as a function of temperature (230≤T≤335 K) for OH/H_2O samples with 4≤λ≤13. i. OH^- hopping distance (2σ) modelled from QENS data for 4≤λ≤13 OH/H_2O samples between 230≤T≤335 K. **j**, Schematic illustration indicating pseudorotational, diffusional and sometimes nanoconfined dynamics of H_2O molecules occurring within hydrated membrane samples over intermediate (6-14 ps) timescales. **k,l**, Scattering profiles for OH/H_2O samples with λ=4 and 13 recorded at 300 K with E_{res}=17.5 (intermediate resolution - IRIS) and 70 (broad resolution - IN6-Sharp) μeV, respectively. The H_2O dynamics give rise to the main Lorentzian contribution with narrower linewidth (light blue shaded) with a significantly broader "background" signal due to polymer relaxations (grey shaded component). **m**, H_2O relaxation timescale determined from QENS linewidths for λ=4 at T=230≤T≤335 K. **n**, Diffusion constants ($cm^2\ s^{-1}$) determined from fitting QENS profiles for mobile H_2O molecules within AEM samples with λ=8-13 plotted as a function of *1000/T*.

Fig. 4 | Intermediate scattering function to investigate relaxation dynamics as a function of their timescale; data for FAD-55 Membrane. a, Scattering profile in the time domain for H_2O-hydrated (λ=4) OH-samples, at 300 K and Q=1.4 $Å^{-1}$. The global fit (red continuous curve) is overlaid across all datasets on the data points (black). **b-d**, Q-dependency of the *I(Q,t)* over the investigated timescales (broad resolution: IN6-Sharp - E_{res}=70 μeV- panel **d**; intermediate resolution: IRIS - E_{res}=7.5 μeV- panel **e**; high resolution: IN16B - E_{res}=0.75 μeV- panel **d**). **e-g**, In panel **e** is presented the temperature dependence for OH-samples H_2O-hydrated (λ=4) between at 230 (red line) and 325 K (purple line); Q=1.4 $Å^{-1}$. Note here that profiles at 280 and 325 K have been obtained only at two energy resolutions (e.g. IRIS and IN16B). Panel **f** represents a highlight of the slow-dynamics process; panel **g** is included to show the deviation from the quadratic dependence of the intermediate scattering function for OH/H_2O sample at λ=4 and T=230 K in the nanosecond timescale. Full details of the analysis are provided in Supplementary text 2.5.

Fig. 5 | From dynamics parameters to AEM performance; data for FAD-55 Membrane. a, Schematic illustration of an alkaline fuel cell and its mode of operation. We illustrate key areas of different water uptake with sketches indicating the main modes of OH^-/H_2O transport. At the anode with higher hydration levels (e.g. λ=13) the transport dynamics are determined by bulk-like water diffusion, whereas lower hydration (e.g. λ=4, that can drop to λ =1 at high current current densities) at the cathode involve OH^- hopping facilitated by the presence of H_2O molecules hydrogen-bonded to the OH^- groups attached to ionomer QA side groups. Within the membrane the faster anionic diffusion within the aqueous component at intermediate hydration (e.g. λ=8) is slowed down by interaction with the polymer. **b**,**c**, Comparison between diffusion coefficient of anionic species, determined from QENS results (black symbols, left axis), and measured ionic conductance (blue symbols, right axis). Data are shown for λ=13 (square symbols in panels **b** and **c**), as well as for λ=10, 8 and 4 (circle, diamond, and crossed diamond, respectively; panel **c**). In panels **b** and **c** black (left) labels refer to diffusion coefficient (D in $cm^2\ s^{-1}$; black symbols); blue (right) labels refer to OH^- conductivity (σ in mS cm^{-1}; blue symbols).

References

1. A. Zlotorowicz, A., Strand, R. V., Burheim, O. S., Wilhelmsen, Ø. & Kjelstrup, S. The permselectivity and water transference number of ion exchange membranes in reverse electrodialysis. *J.Membr. Sci.* **523**, 402-408 (2017).
2. Gottesfeld, S., et al. Anion exchange membrane fuel cells: Current status and remaining challenges. *J. Power Sources* **375**, 170-184 (2018).
3. Varcoe, J. R. et al. Anion-exchange membranes in electrochemical energy systems. *Energy Environ. Sci.* **7,** 3135 (2014).
4. Kumar, S. S & Himabindu, V. Hydrogen production by PEM water electrolysis – A review. *Materials Science for Energy Technologies* **2**, 442-454 (2019).

5. Henkensmeier, D., Najibah, M., Harms, C., Žitka, J., Hnát, J. & Bouzek, K. Overview: State-of-the art commercial membranes for anion exchange membrane water electrolysis. *J. Electrochem. Energy Convers. Stor.* **18**(2), 024001 (2021).
6. Hren, M., Božič, M., Fakin, D., Kleinschek, K. S. & Gorgieva, S. Alkaline membrane fuel cells: anion exchange membranes and fuels. *Sustainable Energy & Fuel* **5**, 604-637 (2021).
7. FuelCellStore. Fumasep FAD-55. https://www.fuelcellstore.com/fuel-cell-components/membranes/anion-exchange-membrane (2020).
8. Barnes, A. M, Liu, B. & Buratto, S. K. Humidity-dependent surface structure and hydroxide conductance of a model quaternary ammonium anion exchange membrane. *Langmuir* **35**, 14188-14193 (2019).
9. Ran, J. et al. Anion exchange membranes (AEMs) based on poly(2,6-dimethyl-1,4-phenylene oxide) (PPO) and its derivatives. *Polym. Chem.* **6**, 5809-5826 (2015).
10. Pusara, S., Srebnik, S. & Dekel, D. R. Molecular simulation of quaternary ammonium solutions at low hydration levels. *J. Phys. Chem. C* **122**, 11204-11213 (2018).
11. Ramaswamy, N. & Mukerjee, S. Alkaline Anion-Exchange Membrane Fuel Cells: Challenges in Electrocatalysis and Interfacial Charge Transfer. *Chem. Rev.* **119**(23), 11945-11979 (2019).
12. S pringer, T. E., Zawodzinski, T. A. & Gottesfeld, S. Polymer Electrolyte Fuel Cell Model. *J. Electrochem. Soc.* **138**, 2334-2342 (1919).
13. Marx, D., Chandra, A. & Tuckerman, M. E. Aqueous basic solutions: hydroxide solvation, structural diffusion, and comparison to the hydrated proton. *Chem. Rev.* **110**, 2174-2216 (2010).
14. T uckerman, M. E., Marx, D. & Parrinello, M. The nature and transport Mechanism of hydrated hydroxide ions in aqueous solution. *Nature* **417**, 925-929 (2002).
15. Dubey, V., Maiti, A. & Daschakraborty, S. Predicting the solvation structure and vehicular diffusion of hydroxide ion in an anion exchange membrane using nonreactive molecular dynamics simulation. *Chem. Phys. Lett.* **755**, 137802 (2020).
16. Chen, C., Tse, Y.-L. S, Lindberg, G. E., Knight, C. & Voth, G. A. Hydroxide solvation and transport in anion exchange membranes. *J. Am. Chem. Soc.* **138**, 991-1000 (2016).
17. Dong, D., Zhang, W., van Duin, A. C. T. & Bedrov, D. Grotthuss versus vehicular transport of hydroxide in anion-exchange membranes: insight from combined reactive and nonreactive molecular simulations. *J. Phys. Chem. Lett.* **9**, 825-829 (2018).
18. Zhang, W., Dong, D., Bedrov, D. & van Duin, A. C. T. Hydroxide transport and chemical degradation in anion exchange membranes: a combined reactive and non-reactive molecular simulation study. *J. Mater. Chem. A* **7**, 5442-5452 (2019).
19. Zelovich, T., et al. Hydroxide ion diffusion in anion-exchange membranes at low hydration: Insights from ab initio molecular dynamics. *Chem. Mater.* **31**, 5778-5787 (2019).
20. Li, X., Yu, Y., Liu, Q. & Meng, Y. Synthesis and characterization of anion exchange membranes based on poly(arylene ether sulfone)s containing various cations functioned tetraphenyl methane moieties. *Int. J. Hydrogen Energy* **38**, 11067-11073 (2013).
21. Diesendruck, C. E. & Dekel, D. R. Water – A key parameter in the stability of anion exchange membrane fuel cells. *Curr. Opin. in Electrochem.* **9**, 173-178 (2018).
22. Dekel, D. R., Amar, M., Willdorf, S., Kosa, M., Dhara, S. & Diesendruck, C. E. Effect of water on the stability of quaternary ammonium groups for anion exchange membrane fuel cell applications. *Chem. Mater.* **29**, 4425-4431 (2017).
23. Lyonnard, S. et al. Perfluorinated surfactants as model charged systems for understanding the effect of confinement on proton transport and water mobility in fuel cell membranes. A study by QENS. *Eur. Phys. J. Spec. Top.* **189**, 205-216 (2010).
24. Perrin, J.-C., Lyonnard, S. & Volino, F. Quasielastic neutron scattering study of water dynamics in hydrated nafion membranes. *J. Phys. Chem. C* **111**, 3393-3404 (2007).
25. Berrod, Q., Hanot, S., Guillermo, A., Mossa, S. & Lyonnard, S. Water sub-diffusion in membranes for fuel cells. *Sci. Rep.* **7**, 8326 (2017).
26. Hanot, S., Lyonnard, S. & Mossa, S. Sub-diffusion and population dynamics of water confined in soft environments. *Nanoscale* **8**, 3314-3325 (2016).
27. FuelCellStore. Fumasep FAD-55. https://www.fuelcellstore.com/fumasep-fad-55 (2020).

28. Dlugolecki, P., Nymeijer, K., Metz, S. & Wessling, M. Current status of ion exchange membranes for power generation from salinity gradients. *J. Membr. Sci.* **319**, 214-222 (2008).
29. McGrath, M. J. et al. 110th Anniversary: The dehydration and loss of ionic conductivity in anion exchange membranes due to $FeCl_4^-$ ion exchange and the role of membrane microstructure. *Ind. Eng. Chem. Res.* **58**, 22250-22259 (2019).
30. Palaty, Z. & Benndová, H. Permeability of a Fumasep-FAD membrane for selected inorganic acids. *Chem. Eng. Technol.* **41**, 385-391 (2018).
31. Marino, M. G., Melchior, J. P., Wohlfarth, A. & Kreuer, K. D. Hydroxide, halide and water transport in a model anion exchange membrane. *J. Membr. Sci.* **464**, 61-71 (2014).
32. Melchior, J.-P., Lohstroh, W., Zamponni, M. & Jalarvo, N.H. Multiscale water dynamics in model anion exchange membranes for alkaline membrane fuel cells. *J. Membr. Sci.* **586**, 240-247 (2019).
33. Melchior, J.-P. & Jalarvo, N.H. A quasielastic neutron scattering study of water diffusion in model anion exchange membranes over localized and extended volume increments. *J. Phys. Chem. C* **123**, 14195-14206 (2019).
34. Wang, L., Peng, X., Mustain, W. E. b & Varcoe, J. R. Radiation-grafted anion-exchange membranes: the switch from low- to high-density polyethylene leads to remarkably enhanced fuel cell performance. *Energy Environ. Sci.* **12**, 1575-1579 (2019).
35. Deavin, O. I. et al. Anion-exchange membranes for alkaline polymer electrolyte fuel cells: comparison of pendent benzyltrimethylammonium- and benzylmethylimidazolium-head-groups. *Energy Environ. Sci.* **5**, 8584-8597 (2012).
36. Yassin, K., Rasin, I. G., Brandon, S. & Dekel, D. R. Quantifying the critical effect of water diffusivity in anion exchange membranes for fuel cell applications. *J.Membr. Sci.* **608**, 118206 (2020).
37. Mandal, M., et al. The importance of water transport in high conductivity and high-power alkaline fuel cells. *J. Electrochem. Soc.* **167**, 054501 (2020).
38. Chempath, S. et al. Mechanism of tetraalkylammonium headgroup degradation in alkaline fuel cell membranes. *J. Phys. Chem. C* **112**, 3179-3182 (2008).
39. Prager, M., Pawlukojc, A., Wischnewski, A. & Wuttke, J. Inelastic neutron scattering study of methyl groups rotation in some methylxanthines. *J. Chem. Phys.* **127**, 214509 (2007).
40. De Petris, S., Frosini, V., Butta, V. & Boccaredda, M. Mechanical relaxation in in poly(2.6-dimethyl-l.4-phenylene oxide) in glassy state. *Die Makromolekulare Chemie* **109**, 54-61 (1967).
41. Ma, Z. & Tuckerman, M. E. On the connection between proton transport, structural diffusion, and reorientation of the hydrated hydroxide ion as a function of temperature. *Chem. Phys. Lett.* **511**, 177-182 (2011).
42. Zadok, I. et al. Unexpected hydroxide ion structure and properties at low hydration. *J. Mol. Liq.* **313**, 113485 (2020).
43. Torell, L. M. & Angell, C. A. Ion-matrix coupling in polymer electrolytes from relaxation time studies. *Br. Polym. J.* **20**, 173-179 (1988).
44. Angell, C. A. Relaxation in liquids, polymers and plastic crystals - strong/fragile patterns and problems. *J. Non-Cryst. Solids* **131-133**, 13-31 (1991).
45. Gotze, W. & Sjogren, L. Relaxation processes in supercooled liquids. *Rep. Prog. Phys.* **55**, 241-376 (1992).
46. Bhattacharyya, S. M., Bagchi, B. & Wolynes, P. G. Facilitation, complexity growth, mode coupling, and activated dynamics in supercooled liquids. *Proc. Natl. Acad. Sci. USA* **105**, 16077-16082 (2008).
47. Dong, D., Wei, X., Hooper, J. B., Pan, H. & Bedrov, D. Role of cationic groups on structural and dynamical correlations in hydrated quaternary ammonium-functionalized poly(p-phenylene oxide)-based anion exchange membranes. *Phys. Chem. Chem. Phys.* **20**, 19350-19362 (2018).
48. Meek, K. M. et al. The alkali degradation of LDPE-based radiation-grafted anion-exchange membranes studied using different ex situ methods. *RSC Adv.* **10**, 36467-36477 (2020).
49. Mustain, W. E., Chatenet, m., Page, M. & Kim, Y. S. Durability challenges of anion exchange membrane fuel cells. *Energy Environ. Sci.* **13**, 2805-2838 (2020).
50. Ziv, N., Mustain, W. E. & Dekel, D. R. The effect of ambient carbon dioxide on anion-exchange membrane fuel cells. *ChemSusChem* **11**, 1136-1150 (2018).

51. Dekel, D. R., Rasin, I. G., Page, M. & Brandon, S. Steady state and transient simulation of anion exchange membrane fuel cells. *J. Power Sources* **375**, 191-204 (2018).
52. Zheng, Y. et al. Water uptake study of anion exchange membranes. *Macromolecules* **51**, 3264-3278 (2018).

Materials and Methods

Membrane materials and sample preparation

Fumasep FAD-55 Anion Exchange Membranes (AEM) were purchased as 10×10 cm sheets with 50-60 µm thickness from FuMA-Tech GmbH (Bietigheim, Germany). These polymer materials are designed to have high ionic conductance combined with mechanical and chemical stability at pH<9. The membrane package was kept sealed until ready for use. The as-received membranes were treated in aqueous NaCl (1 wt%) at 25°C for 24 h and subsequently washed repeatedly in ultrapure water to remove the salt, demonstrated by testing the conductivity of the washing water.

Samples were examined in Br- (to minimise the signal from Br- during the neutron experiments) and Cl-forms (to best directly compare the QENS and conductivity results) as well as substituted with OH^-. The ionic forms (OH^-, $Br^-$and/or Cl^-) were produced by immersing in 1 M NaOH, NaBr (aq), or NaCl (aq) at room temperature for 1h, changing the solution three times to ensure the complete ion-exchange. Each sample was washed repetitively in ultrapure water to remove excess NaOH (NaBr or NaCl), as established by testing the conductivity of the washing water.

Experiments were carried out on three H/D isotopically substituted compositions at water contents ranging between high (λ=13) and low (λ=4) hydration levels expressed as the number of water molecules per functional group. The highest λ was obtained by first immersing the membrane in liquid water followed by gentle pad-drying to remove excess liquid; lower hydration was obtained by removing the appropriate amount of water using a vacuum oven (Room Temperature) and heating for specified times followed by weighing. Further low-hydrated samples ($\lambda \leq 2$) were obtained by heating overnight (≥10 h) in a vacuum oven at T=40°C.

HDPE-VBC-TMA membranes with high alkaline stability and OH^- conductivity designed for AEMFC technology were produced at the University of Surrey [34]. These samples were tested in OH-form in H_2O (following the ion-exchange procedure described above) at λ=4.

Quasi-elastic neutron scattering (QENS) experiments

Four QENS spectrometers at three instrument facilities were used: i) IN6-Sharp (ILL, France), to investigate relaxation dynamics on a ps time scale; ii) IRIS (ISIS, UK), to study dynamics on the tens to hundred ps-time scale; and iii-iv) IN16B (ILL, France) as well as the High Flux Backscattering Spectrometer (HFBS; NIST, USA) to investigate ns timescales. Employing spectrometers that access different timescales was necessary to carry out a full characterization of the sample dynamics.

TOF experiments were performed at 300 K using an incident wavelength of λ=5.12 Å (covering a Q-range between 0.3-2.1 $Å^{-1}$) and an instrument energy resolution of 70 µeV (E_{res}; obtained by measuring the reference sample at 2 K); this configuration allows probing motions in the ps time scale of $0.5<\tau<20$ ps. Complementary experiments were performed from 230-325 K on IRIS, using the PG002 analyser crystal set-up ($0.56 \leq Q \leq 1.84$ $Å^{-1}$) and E_{res} of 17.5 µeV, probing motions in the in the range $5<\tau<100$ ps. IN16B experiments were performed using the standard unpolished strained Si(111) monochromator and analyser

corresponding to an incident wavelength of λ=6.271 Å (covering a Q-range between 0.56 and 1.79 $Å^{-1}$), an instrument energy resolution of 0.75 μeV, and a dynamic range of ±30 μeV; HFBS experiments were performed over a Q range of 0.25 to 1.75 $Å^{-1}$, with E_{res}=1.0 μeV and a dynamic range of ±15 μeV. These two spectrometers probe motions in the ns time scale (0.07<τ<3 ns). Any dynamical process with longer characteristic timescale will appear as 'elastic' scattering (i.e., contained within the E_{res} profile) in the QENS profile, while faster processes that are accessible to the instrument contribute to a background in the QENS dataset.

Elastic fixed window scans (EFWS) were recorded while heating (0.13 K min^{-1}; from 2 to 300/325 K; IN6-Sharp and IN16B, respectively) or cooling (IRIS) the sample. Inelastic fixed window scans (IFWSs) were recorded either by adjusting the Doppler speed on IN16B to achieve ΔE=3 and 6 μeV energy offsets, or integrating an arbitrarily chosen energy range (having integration width equivalent to E_{res}; IRIS and IN6-Sharp).

AEM samples were wrapped in Al foil and then loaded into In sealed either in Au-coated flat cell (4×5 cm) or Al annular cells. In both cases the cells had an inner thickness of ~0.5 mm to achieve a neutron transmission of ~90%, minimising multiple scattering. Vanadium reference and empty can measurements were carried out for data normalization (e.g. detector efficiency corrections and/or data normalisation to absolute units).

Ionic conductivity measurements (OH^- and Cl^- anions, partially to fully hydrated)

The ionic conductivity for FAD-55 membrane was tested for both ionic forms (OH^- and Cl^-) under fully (100% RH) and partially (80≤RH≤65) hydrated conditions in the temperature range from 303 to 353 K, using a BekkTech four-point probe conductivity cell.

Sample characterisation

FTIR spectra were recorded on a Bruker Alpha FTIR instrument between 400-4000 cm^{-1} for 16 averaged scans at 0.25 cm^{-1} resolution with autosubtracted background. AFM images were recorded using Bruker Dimension Icon with SNL-10A and Scanasyst fluid+ probe. Sample imaging in water was carried out in PeakForce tapping mode. Thermogravimetric analysis (TGA) was performed on a Mettler Toledo TGA/DSC 1. Samples (~5 mg) in a ceramic pan were heated from 50-600°C at 10 °C min^{-1} under 60 mL min^{-1} flowing N_2, taking measurements at 1s intervals. The raw TGA thermograms were corrected by subtraction of an empty pan measurement, and normalised to their weight at 50°C. Prior to IEC analysis, samples in Cl-form were vacuum dried at 50°C for 4 h and the dry mass (m_d; g) recorded using a Metler Toledo Model MS204S analytical balance. Individual samples were separately immersed in aqueous $NaNO_3$ (20 cm^3, 1.2 mol dm^{-3}, large excess of NO_3^- anions) and the solutions were stirred overnight at 200 rpm to exchange the Cl^- with NO_3^-. Before titration HNO_3 (1 cm^3, 2 mol dm^{-3}) was added to the $NaNO_3$ solutions. Each solution was titrated with $AgNO_3$ (20.00 ± 0.06 mmol dm^{-3}) using the Metrohm 848 Titirino plus auto titrator equipped with Ag-Titrode. The IEC of each sample (mmol g^{-1}) was calculated from end-point volume (EP; cm^3) and $AgNO_3$ concentration using: $IEC = (EP \times 0.02) / m_d$ [34]. Raman spectra (for samples treated as described for IEC determination) were recorded using an InVia Reflex Raman Microscope (Renishaw, UK). Spectra were recorded on five random spots on each sample surface using 785 nm excitation (100 % laser power with pin in to create a spot), a 20 × objective lens (NA = 0.40) and 0.5 s exposure time. To reduce background fluorescence and improve the signal-to-noise ratio, each spectrum was acquired with a minimum photobleach of 120 s and an accumulation time of 500 s. The five spectra recorded for each sample were baseline corrected, normalized to the intensity of 1300 cm^{-1} peak (PPO polymer backbone) and averaged to produced a single spectrum per sample.

Small and Wide Angle X-ray (SAXS/WAXS) and Neutron Scattering (SANS)

SAXS/WAXS profiles were acquired on a Nano-inXider instrument (Xenocs, Sassenage, France) using a micro-focus sealed-tube Cu 30 W/30 µm X-ray source (Cu K-α, λ=1.54 Å). The SAXS/WAXS scattering patterns (covering Q-ranges 0.0045-0.37 $Å^{-1}$ and 0.3-4.1 $Å^{-1}$, respectively) were detected simultaneously using two Dectris Pilatus 3 hybrid pixel detectors. Scattering was collected on the same samples measured with SANS and loaded in sealed capsules with kapton windows, at room temperature and humidity. The WAXS profiles were de-convoluted using Origin2019b. SANS measurements were performed on the SANS2d beamline at the ISIS Pulsed Neutron & Muon Source (STFC Rutherford Appleton Laboratory, UK), using neutrons with wavelengths of $1.65 \leq \lambda \leq 14$ Å. Scattering profiles were simultaneously recorded on 2 two-dimensional detectors positioned at 4 and 8 m from the sample; providing a wide scattering vector ($Q=(4\pi/\lambda)\sin\vartheta$) range $0.0025 \leq Q \leq 0.8$ $Å^{-1}$. FAD membranes were investigated after overnight treatment either (i) in vacuum oven at 40°C (λ=2) or ii) immersed in liquid H_2O and removing the excess of surface water pad drying the membrane surface (e.g. hydrated samples). All measurements were performed in sealed 1 mm thick fused quartz Hellma cells at 25°C and room humidity.

Data and materials availability: All data needed to evaluate the conclusions in the paper are present in the paper and/or the Supplementary Materials. Source data are available at DOI: 10.5286/ISIS.E.RB1920608, 10.5286/ISIS.E.RB2090038-1 and 10.5291/ILL-DATA.9-11-1916, and provided as a Source Data file. Additional data related to this paper may be requested from the authors.

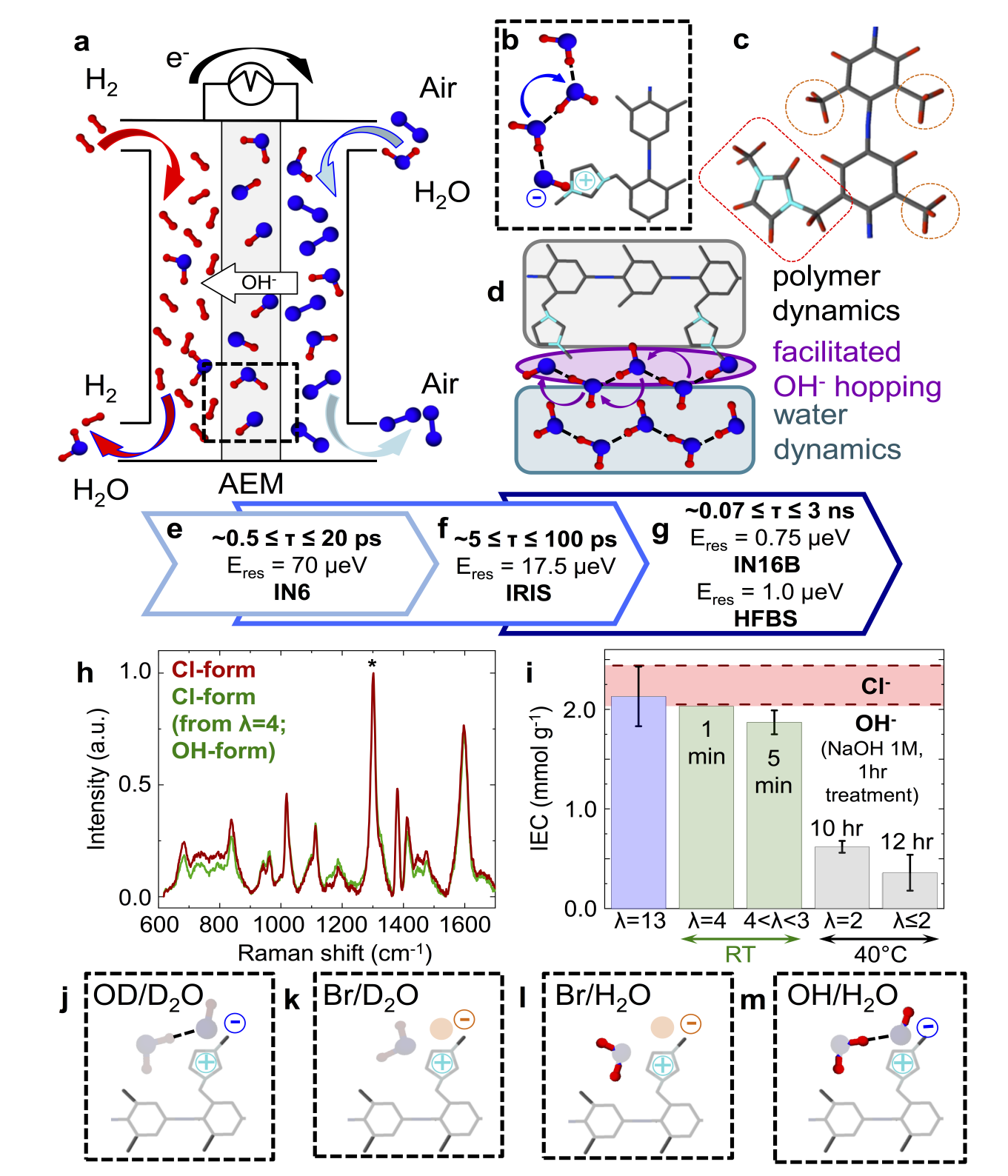
a
e⁻
H2
Air
H2O
OH⁻
H2
Air
H2O
AEM
b
c
d
polymer dynamics
facilitated OH⁻ hopping
water dynamics
e ~0.5 ≤ τ ≤ 20 ps
Eres = 70 μeV
IN6
f ~5 ≤ τ ≤ 100 ps
Eres = 17.5 μeV
IRIS
g ~0.07 ≤ τ ≤ 3 ns
Eres = 0.75 μeV
IN16B
Eres = 1.0 μeV
HFBS
h
Cl-form
Cl-form (from λ=4; OH-form)
Intensity (a.u.)
Raman shift (cm⁻¹)
i
Cl⁻
OH⁻ (NaOH 1M, 1hr treatment)
IEC (mmol g⁻¹)
1 min
5 min
10 hr
12 hr
λ=13
λ=4
4<λ<3
λ=2
λ≤2
RT
40°C
j OD/D2O
k Br/D2O
l Br/H2O
m OH/H2O

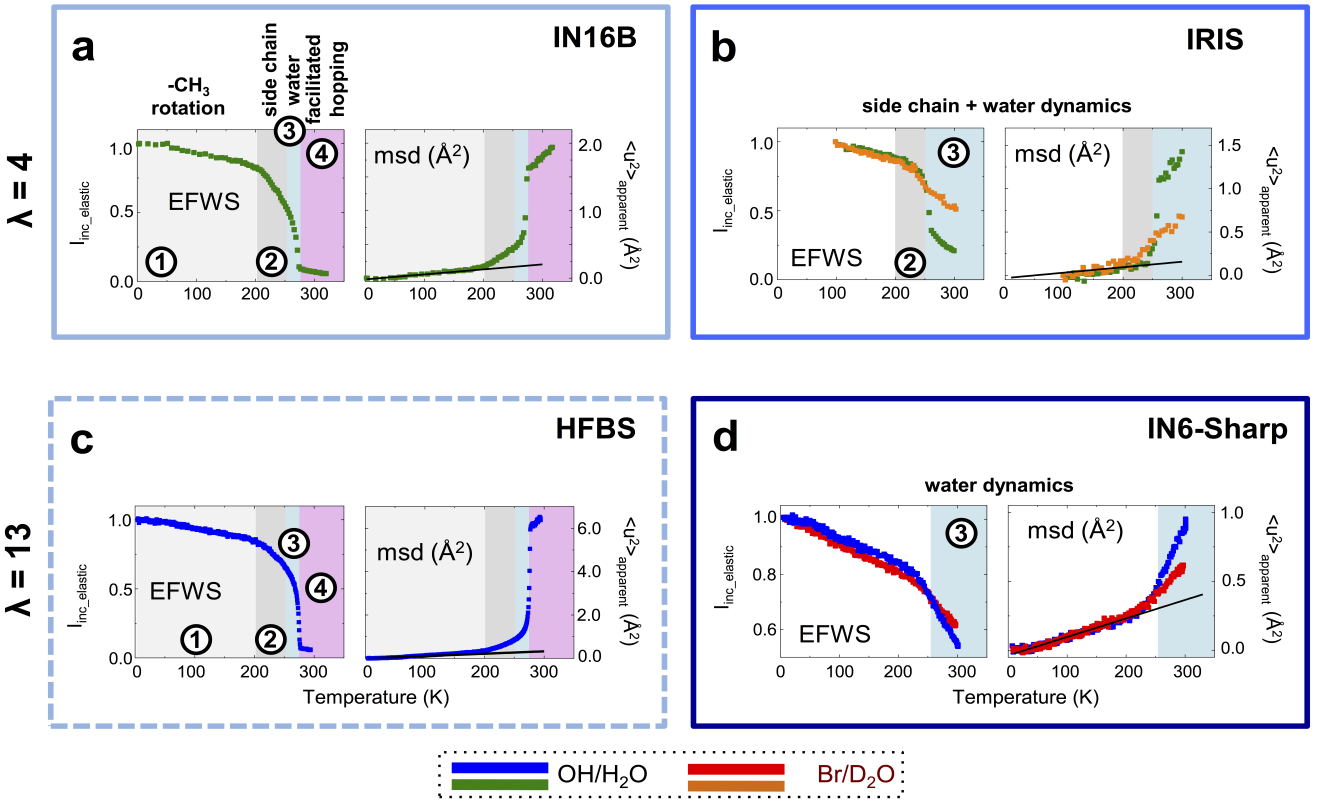
λ = 4
λ = 13
a
IN16B
-CH3 rotation
side chain water facilitated hopping
EFWS
msd (Å2)
Iinc_elastic
<u2>apparent (Å2)
b
IRIS
side chain + water dynamics
c
HFBS
d
IN6-Sharp
water dynamics
Temperature (K)
OH/H2O
Br/D2O

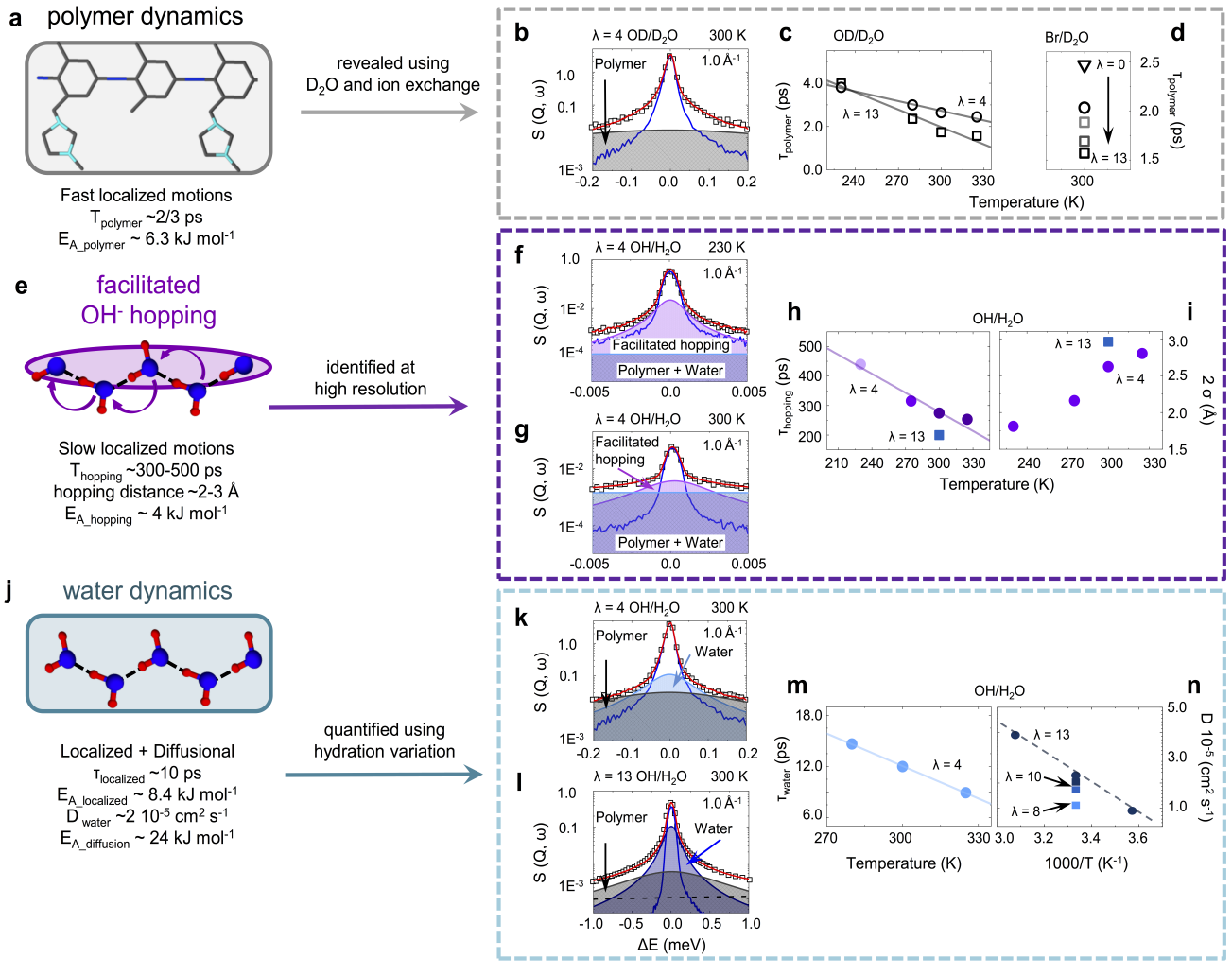
a
polymer dynamics
revealed using
D2O and ion exchange
Fast localized motions
Tpolymer ~2/3 ps
EA_polymer ~ 6.3 kJ mol-1
b
λ = 4 OD/D2O
300 K
Polymer
1.0 Å-1
S (Q, ω)
c
OD/D2O
Br/D2O
λ = 13
λ = 4
λ = 0
Tpolymer (ps)
Temperature (K)
d
Tpolymer (ps)
e
facilitated
OH- hopping
identified at
high resolution
Slow localized motions
Thopping ~300-500 ps
hopping distance ~2-3 Å
EA_hopping ~ 4 kJ mol-1
f
λ = 4 OH/H2O
230 K
Facilitated hopping
Polymer + Water
g
λ = 4 OH/H2O
300 K
h
OH/H2O
Thopping (ps)
i
2 σ (Å)
j
water dynamics
Localized + Diffusional
τlocalized ~10 ps
EA_localized ~ 8.4 kJ mol-1
D water ~2 10-5 cm2 s-1
EA_diffusion ~ 24 kJ mol-1
quantified using
hydration variation
k
λ = 4 OH/H2O
300 K
Water
l
λ = 13 OH/H2O
300 K
ΔE (meV)
m
OH/H2O
Twater (ps)
n
D 10-5 (cm2 s-1)
1000/T (K-1)

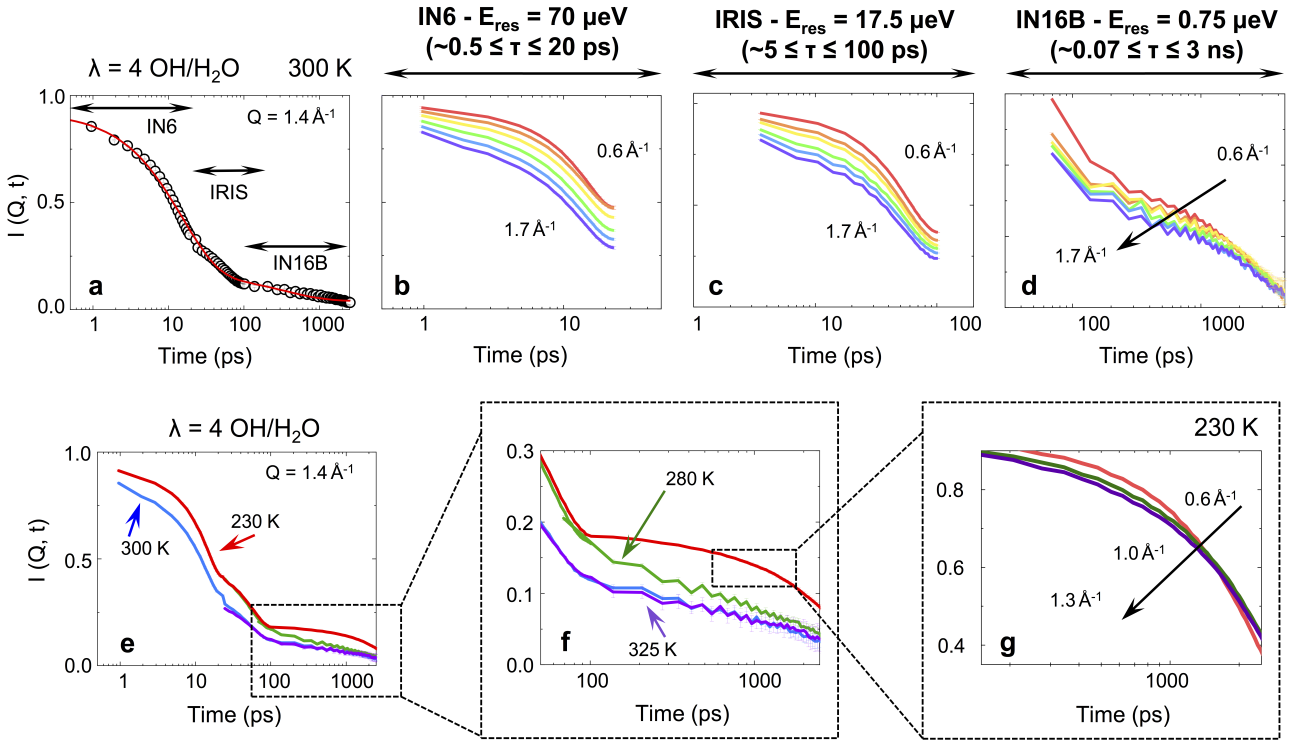
λ = 4 OH/H2O
300 K
IN6 - Eres = 70 μeV
(~0.5 ≤ τ ≤ 20 ps)
IRIS - Eres = 17.5 μeV
(~5 ≤ τ ≤ 100 ps)
IN16B - Eres = 0.75 μeV
(~0.07 ≤ τ ≤ 3 ns)
I (Q, t)
Time (ps)
Q = 1.4 Å-1
IN6
IRIS
IN16B
a
0.6 Å-1
1.7 Å-1
b
c
d
λ = 4 OH/H2O
Q = 1.4 Å-1
300 K
230 K
e
280 K
325 K
f
230 K
0.6 Å-1
1.0 Å-1
1.3 Å-1
g

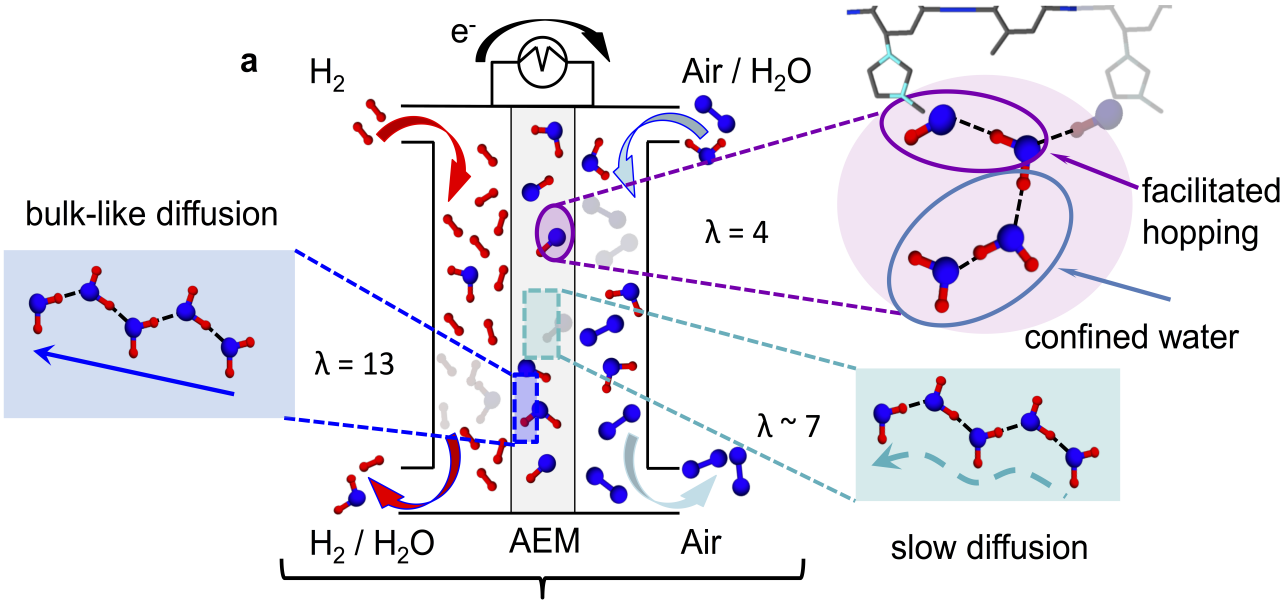
a
e-
H2
Air / H2O
bulk-like diffusion
λ = 13
λ = 4
λ ~ 7
facilitated
hopping
confined water
slow diffusion
H2 / H2O
AEM
Air

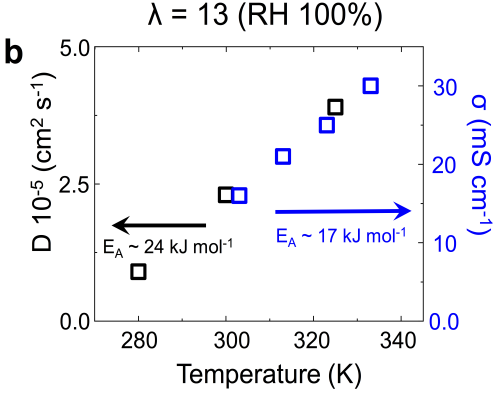
λ = 13 (RH 100%)
b
D 10-5 (cm2 s-1)
σ (mS cm-1)
EA ~ 24 kJ mol-1
EA ~ 17 kJ mol-1
Temperature (K)

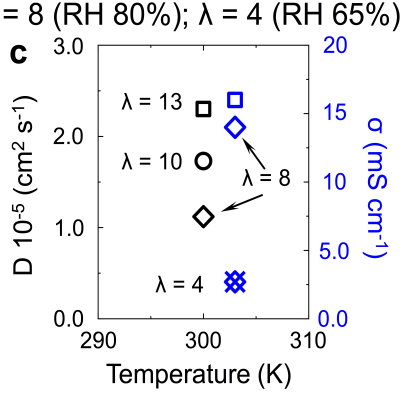
λ = 8 (RH 80%); λ = 4 (RH 65%)
c
D 10-5 (cm2 s-1)
σ (mS cm-1)
λ = 13
λ = 10
λ = 8
λ = 4
Temperature (K)